A Common Explosion Mechanism for Type Ia Supernovae

Paolo A. Mazzali[1,2,3,4*], Friedrich K. Röpke[1,5],
Stefano Benetti[6], and Wolfgang Hillebrandt[1]

[1]Max-Planck Institut für Astrophysik,
Karl-Schwarzschildstr.1, 85748 Garching, Germany
[2]Department of Astronomy, School of Science,
University of Tokyo, Bunkyo-ku, Tokyo 113-0033, Japan
[3]Research Center for the Early Universe, School of Science,
University of Tokyo, Bunkyo-ku, Tokyo 113-0033, Japan
[4]Istituto Nazionale di Astrofisica-OATs, Via Tiepolo 11, I-34131 Trieste, Italy
[5]Department of Astronomy and Astrophysics, University of California Santa Cruz,
1156 High Street, Santa Cruz, CA 95064, U.S.A.
[6]Istituto Nazionale di Astrofisica-OAPd,
vicolo dell'Osservatorio, 2, I-35122 Padova, Italy

*To whom correspondence should be addressed; E-mail: mazzali@ts.astro.it

Type Ia supernovae, the thermonuclear explosions of white dwarf stars composed of carbon and oxygen, were instrumental as distance indicators in establishing the acceleration of the universe's expansion. However, the physics of the explosion are debated. Here we report a systematic spectral analysis of a large sample of well observed type Ia supernovae. Mapping the velocity distribution of the main products of nuclear burning, we constrain theoretical scenarios. We find that all supernovae have low-velocity cores of stable iron-group elements. Outside this core, nickel-56 dominates the supernova ejecta. The outer extent of the iron-group material depends on the amount of nickel-56 and coincides with the inner extent of silicon, the principal product of incomplete burning. The outer extent of the bulk of silicon is similar in all SNe, having an expansion velocity of $\sim 11000\,\mathrm{km\,s^{-1}}$ and corresponding to a mass of slightly over one solar mass. This indicates that all the supernovae considered here burned similar

masses, and suggests that their progenitors had the same mass. Synthetic light curve parameters and three-dimensional explosion simulations support this interpretation. A single explosion scenario, possibly a delayed detonation, may thus explain most type Ia supernovae.

When a white dwarf (WD) composed of carbon and oxygen accreting mass from a companion star in a binary system approaches the Chandrasekhar mass [$M_{\rm Ch} \approx 1.38$ solar masses ($M_\odot$)], high temperature causes the ignition of explosive nuclear burning reactions that process stellar material and produce energy. The star explodes leaving no remnant, producing a Type Ia supernova (SNIa) (*1*). At high stellar material densities, burning yields nuclear statistical equilibrium (NSE) isotopes, in particular radioactive ^{56}Ni which decays to ^{56}Co and ^{56}Fe making the SN bright (*2*). At lower densities intermediate mass elements (IME) are synthesised. Both groups of elements are observed in the optical spectra of SNeIa (*3*). An empirical relation between an observed quantity, the B-magnitude decline over the first 15 days after maximum luminosity [$\Delta m_{15}(B)$] and a physical quantity, the SN maximum luminosity (*4*), can be used to determine the distance to a SNIa. This method was applied to very distant SNeIa leading to the discovery of the accelerating Universe (*5,6*). How the explosion actually proceeds is however debated (*7,8,9*), as is the nature of the progenitor system: Accretion may occur either from a more massive companion (e.g. a giant) or via the merging of two carbon-oxygen WDs (*10*). This casts a shadow on the reliability of SNeIa as distance indicators, as intrinsically very different explosions may result in the observed correlation.

We derive the distribution of the principal elements in 23 nearby SNeIa (distances <40 Mpc) with good spectral coverage extending from before maximum to the late nebular phase, about one year later. The sample (table S1) covers a wide range of light-curve decline rates and includes peculiar objects like SN2000cx, which violates the luminosity-decline-rate relation.

Because of the hydrodynamic properties of the explosion, the expansion velocity of the ejecta is proportional to radius and serves as a radial coordinate. As the SN expands, deeper layers are exposed. The outer layers, visible in the first few weeks after the explosion, are dominated by IME. Because silicon is the most abundant IME, we measured its characteristic expansion velocity from the blueshift of the absorption core of the strong SiII 6355 Å line in all spectra where it was visible. This velocity decreases with time. Fitting the postmaximum velocity evolution and extrapolating it to the earliest times, when the outermost parts of the ejecta are visible, we derived the outer extension of the bulk of Si. This represents a lower limit of the outer extent of burning. The Si velocity v(Si) is similar in all SNeIa, regardless of their luminosity: $v(\mathrm{Si}) = 11900 \pm 1300\,\mathrm{km\,s^{-1}}$.

A few SNe, defined as High Velocity Gradient (HVG) SNe (*11*), are responsible for most of the dispersion. They have a rapidly decreasing v(Si) before maximum and very high-velocity CaII lines, possibly the result of high-velocity blobs that carry little mass and kinetic energy but cause High-Velocity absorption Features (HVF, (*12*)) that can abnormally broaden the SiII line profile (*12,13*). Although excluding them from the sample decreases the dispersion in v(Si) significantly [$v(\mathrm{Si}) = 11300 \pm 650\,\mathrm{km\,s^{-1}}$], we include all these SNe in our discussion.

The maximum Si velocity thus measured is a conservative estimate. The deep absorption core is produced in layers of high silicon abundance. Silicon is present at higher velocities, indicated by the wavelength of bluest absorption in the earliest spectrum of each SN. However, measuring the bluest absorption velocity yields a large scatter because the earliest spectra have different epochs and may be affected by HVFs (*12*). Our method reliably determines the outer location of the bulk of IMEs.

The inner extent of Si, determined from the asymptotic velocity of the SiII 6355 Å line in post-

maximum spectra [fig. 1 in (*11*)], is a steep function of $\Delta m_{15}(B)$. The brightest (slowest declining) SNe have the thinnest Si zones.

The inner ejecta, dominated by NSE elements, are best observed ~1 year after the explosion, when dilution caused by expansion makes the SN behave like a nebula, exposing the deepest layers. Collisions with the fast particles produced by the decay $^{56}\mathrm{Ni} \rightarrow {}^{56}\mathrm{Co} \rightarrow {}^{56}\mathrm{Fe}$ heat the gas, which cools emitting radiation mostly in forbidden lines.

We modeled the nebular spectra using a code that computes line emission balancing heating and cooling in non-local thermodynamic equilibrium (NLTE) (*14*), including density and abundance stratification. We adopted the density-velocity distribution of the standard, one-dimensional, M_{Ch} explosion model W7 (*1*), (fig. S1). In the nebular phase the gas is transparent, and line emissivity depends on the mass of the emitting ion. Accurately estimating this mass requires determining the ionization state of the gas. Forbidden lines of FeII and FeIII dominate SNIa nebular spectra, reflecting the high abundance of NSE material. Fe is mostly the product of ^{56}Ni decay, which provides heating. The stable, neutron-rich isotopes ^{54}Fe and ^{58}Ni do not contribute to heating, but do contribute to cooling, because they also emit forbidden lines. Their presence affects the ionization balance. Both are mostly produced deep in the WD, at the highest densities. The ^{54}Fe nebular lines have wavelengths indistinguishable from those of ^{56}Fe.

We determined the mass and distribution in velocity of the Fe isotopes (and thus of ^{56}Ni) simultaneously fitting the ratio of the two strongest Fe emissions(fig. S1). One, near 4700 Å includes both FeII and FeIII lines, while the other, near 5200 Å, is only due to FeII. A low upper limit to the mass of ^{58}Ni is set by the absence of strong emission lines (in particular at 7380 Å).

In the deepest layers (Fig. 1), all SNe contain ~0.1 to 0.3 $M_{\odot}$ of stable NSE isotopes, with a large scatter and no dependence on $\Delta m_{15}(B)$ [see also (*15*)].

As expected, the ^{56}Ni mass correlates inversely with $\Delta m_{15}(B)$, ranging from 0.9 $M_{\odot}$ for the slowest declining (most luminous) SNe to 0.1 $M_{\odot}$ for the fastest declining (dimmest) ones. The root mean square (rms) dispersion is 0.13 $M_{\odot}$, but SNe with intermediate decline rates [$\Delta m_{15}(B) \sim 1.05$ to 1.5 magnitudes] show variations of almost a factor of 2 for the same value of $\Delta m_{15}(B)$. These SNe could cause scatter about the mean luminosity-decline-rate relation (*16*).

Once the contributions of ^{56}Ni, ^{54}Fe, and ^{58}Ni are added together to evaluate the total NSE mass, the dispersion decreases to 0.09 $M_{\odot}$. If SNe with different amounts of ^{56}Ni, and thus presumably different temperatures, but similar NSE content have similar $\Delta m_{15}(B)$, it is likely that abundances (*17*) rather than temperature (*18*) primarily determine the opacity and light-curve shape.

The outer velocity of the NSE region, determined from the width of the Fe lines, correlates with SN luminosity (*19*). It coincides with the innermost silicon velocity, marking the transition from complete to incomplete burning: the difference between these two velocities, $\Delta(v) = 650 \pm 900\,\mathrm{km\,s^{-1}}$, is consistent with zero. Remarkably, this results from two different methods applied to data obtained almost 1 year apart.

Thus, while the mass of ^{56}Ni, and consequently the SN luminosity, can differ significantly, other characteristics of SNeIa are remarkably homogeneous. In particular, the narrow dispersion of the outer Si velocity indicates a similar extent of thermonuclear burning in all SNeIa: SNe that produce less ^{56}Ni synthesize more IMEs.

The simplest interpretation of these seemingly antithetic results is that thermonuclear burning consumes similar masses in all SNeIa. We explore whether this scenario is consistent with the M_{Ch} model (*10*). Applying the density-velocity structure of model W7 (*1*), we transform v(Si) to mass (Fig. 1).

Table 1: Results and DDT parameters of parametrized three-dimensional delayed detonation models.

model	$E_{\rm kin}^{\rm asympt}$ ($10^{51} erg$)	M(NSE) ($M_\odot$)	M(IME) ($M_\odot$)	$t_{\rm DDT}$ (s)	$\rho_{\rm DDT}$ (10^7 g cm^{-3})
D800	1.004	0.638	0.547	0.675	2.40
D20	1.237	0.833	0.435	0.724	1.92
D5	1.524	1.141	0.220	0.731	1.33

We find that the outer shell of silicon encloses a mass of at least $\sim 1.05 \pm 0.09\, M_\odot$ ($\sim 1.01 \pm 0.05\, M_\odot$, excluding HVG SNe), independently of $\Delta m_{15}(B)$. This is a lower limit to the burned mass.

The light-curve width τ is related to $\Delta m_{15}(B)$ (*20*) and depends on the ejected mass $M_{\rm ej}$, the kinetic energy $E_{\rm k}$, and the opacity κ as $\tau \propto \kappa^{1/2} E_{\rm k}^{-1/4} M_{\rm ej}^{3/4}$ (*21*). We test our assumption computing parametrized light-curve widths and comparing them to observed values. The resulting luminosity-decline-rate relation (Fig. 2) is very tight, and practically identical to the observed one. This result supprots our opacity parametrization, corroborating our hypothesis that the mass burned is similar in all SNeIa. Given its weak dependence on $E_{\rm k}$, the light-curve width is not much affected if more of the outer part of the WD is burned to IME, as these do not contribute much to the opacity.

If SNeIa burn a similar mass, the progenitor mass is also likely to be the same, namely $M_{\rm Ch}$. Because the outcome of the burning depends essentially on fuel density, a variation in iron-group elements production in $M_{\rm Ch}$ WDs requires different WD expansion histories. This in turn depends on the details of the burning. Once the WD reaches $M_{\rm Ch}$, a thermonuclear flame is ignited near the center. The flame must start as a subsonic deflagration (*1*), mediated by microphysical transport and accelerated by turbulence. As it propagates outwards, it could undergo a deflagration-to-detonation transition (DDT) and continue as a shock-driven supersonic detonation wave, in a so-called delayed detonation (*22*). This constitutes the most extreme explosion scenario admissible, exploring the limits of $M_{\rm Ch}$ explosions.

We modeled the explosion using a three-dimensional level-set approach (*23*). The ignition of the deflagration flame was treated as a stochastic process generating a number of ignition spots placed randomly and isotropically within 180 km of the WD centre (*24*).

What would cause the DDT is unclear. We assumed that it occurs as turbulence penetrates the internal flame structure: the onset of the so-called distributed burning regime (*25*). This happens at low fuel densities, after some WD pre-expansion in the deflagration phase. The detonation is triggered artificially where the chosen DDT criterion is first satisfied, typically near the outer edges of the deflagration structure (Table 1 shows DDT parameters). Three simulations, with 800, 20, and 5 ignition spots, termed D800, D20, and D5, respectively, were performed on a moving cellular Cartesian grid (*26*) comprising the full star. Model D800, with its dense distribution of ignition points, exhausts the carbon-oxygen fuel at the WD centre almost completely in the deflagration phase. The energy release quickly expands the star, and the subsequent detonation mainly transforms low density outer material to IME. In contrast, the few ignition spots of model D5 consume little material during the deflagration, leaving more fuel at high densities which is converted mostly to NSE isotopes in the vigorous detonation phase. Model D20 provides an intermediate case.

The ejecta compositions of the model explosions agree grossly with the results derived from the spectra. The NSE mass produced ranges from 0.638 to 1.141 $M_\odot$. The weakest explosions result from optimal burning in the deflagration phase (*26*), and subluminous SNeIa are not reached in our parametrization. However, the conditions for DDT need further investigation. Eventually these events may be explained

within a single framework. Some extremely luminous SNeIa may come from very rapidly rotating WDs whose mass exceeds (*27*), but these are rare.

The distribution derived from observations of burning products inside SNeIa could result from the variation of a single initial parameter, the flame ignition configuration, in M_{Ch} delayed detonations. The luminosity-decline-rate relation can be reproduced using this distribution and a simple opacity parametrization. Our results support the M_{Ch} scenario for most SNeIa, adding confidence to their use as distance indicators.

References and Notes

1. K. Nomoto, F.-K. Thielemann, K. Yokoi, *ApJ* **286**, 644 (1984).
2. M. J. Kuchner, R. P. Kirshner, P. A. Pinto, B. Leibundgut, *ApJ* **426**, L89 (1994).
3. D. Branch, J. B. Doggett, K. Nomoto, F.-K. Thielemann, *ApJ* **294**, 619 (1985).
4. M. M. Phillips, *ApJ* **413**, L105 (1993).
5. A. G. Riess, *et al.*, *AJ* **116**, 1009 (1998).
6. S. Perlmutter, *et al.*, *ApJ* **517**, 565 (1999).
7. M. Reinecke, W. Hillebrandt, J. C. Niemeyer, *A&A* **391**, 1167 (2002).
8. V. N. Gamezo, A. M. Khokhlov, E. S. Oran, *Physical Review Letters* **92**, 211102 (2004).
9. T. Plewa, A. C. Calder, D. Q. Lamb, *ApJ* **612**, L37 (2004).
10. W. Hillebrandt, J. C. Niemeyer, *ARA&A* **38**, 191 (2000).
11. S. Benetti, *et al.*, *ApJ* **623**, 1011 (2005).
12. P. A. Mazzali, *et al.*, *ApJ* **623**, L37 (2005).
13. M. Tanaka, P. A. Mazzali, K. Maeda, K. Nomoto, *ApJ* **645**, 470 (2006).
14. P. A. Mazzali, K. Nomoto, F. Patat, K. Maeda, *ApJ* **559**, 1047 (2001).
15. S. E. Woosley, D. Kasen, S. Blinnikov, E. Sorokina, *ArXiv Astrophysics e-prints astro-ph/0609562* (2006).
16. P. A. Mazzali, P. Podsiadlowski, *MNRAS* **369**, L19 (2006).
17. P. A. Mazzali, *et al.*, *ApJ* **547**, 988 (2001).
18. D. Kasen, S. E. Woosley, *astro-ph/0609540* (2006).
19. P. A. Mazzali, E. Cappellaro, I. J. Danziger, M. Turatto, S. Benetti, *ApJ* **499**, L49 (1998).
20. G. Goldhaber, *et al.*, *ApJ* **558**, 359 (2001).

21. W. D. Arnett, *ApJ* **253**, 785 (1982).

22. A. M. Khokhlov, *A&A* **245**, 114 (1991).

23. I. Golombek, J. C. Niemeyer, *A&A* **438**, 611 (2005).

24. S. E. Woosley, S. Wunsch, M. Kuhlen, *ApJ* **607**, 921 (2004).

25. J. C. Niemeyer, S. E. Woosley, *ApJ* **475**, 740 (1997).

26. F. K. Röpke, W. Hillebrandt, J. C. Niemeyer, S. E. Woosley, *A&A* **448**, 1 (2006).

27. D. A. Howell, *et al.*, *Nature* **443**, 308 (2006).

28. M. Stritzinger, B. Leibundgut, *A&A* **431**, 423 (2005).

29. G. Contardo, B. Leibundgut, W. D. Vacca, *A&A* **359**, 876 (2000).

30. A. W. A. Pauldrach, *et al.*, *A&A* **312**, 525 (1996).

31. We thank Elena Pian and Daniel Sauer for help with data analysis.
This work was partly supported by the European Union's Human Potential Programme under contract HPRN-CT-2002-00303, "The Physics of Type Ia Supernovae".

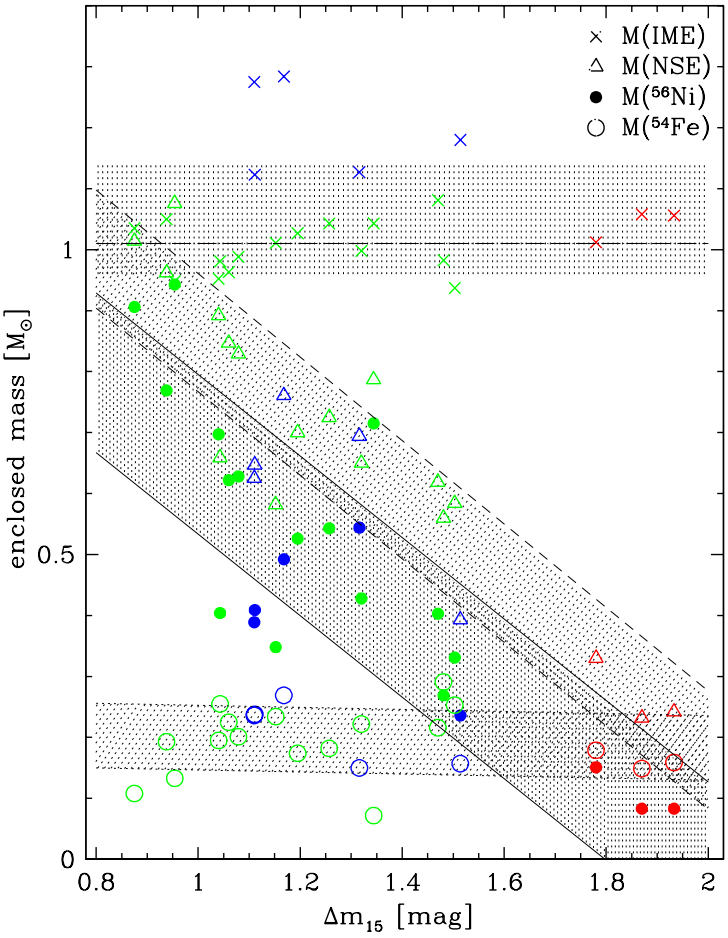

Figure 1: The Zorro Diagram: Distribution of the principal isotopic groups in SNeIa. The enclosed mass (linked to velocity via the W7 explosion model) of different burning products is shown versus decline-rate parameter $\Delta m_{15}(B)$ (a proxy for SN luminosity). Individual SNe are coloured according to their velocity evolution (*11*): HVG, blue; low velocity gradient (LVG), green; and faint, red. Open circles indicate the mass of stable ^{54}Fe+^{58}Ni for each SN; solid circles that of ^{56}Ni, and open triangles the sum of these (total NSE mass). Crosses show the sum of NSE and IME mass, indicating the total mass burned. The IME mass is the difference between crosses and triangles. ^{54}Fe and ^{58}Ni are found in roughly constant amounts in the deepest parts of all SNe, irrespective of luminosity: M(stableNSE) = 0.20 ± 0.05 $M_\odot$ (lower horizontal shaded area). The ^{56}Ni mass determines the SN luminosity. It correlates with $\Delta m_{15}(B)$: $M(^{56}\mathrm{Ni}) = 1.34 - 0.67\Delta m_{15}(B)[M_\odot]$, with rms dispersion 0.13 $M_\odot$ (lower diagonal shaded area). The total NSE mass correlates with $\Delta m_{15}(B)$ better than M(^{56}Ni): $M(\mathrm{NSE}) = 1.55 - 0.69\Delta m_{15}(B)[M_\odot]$, rms dispersion 0.09 $M_\odot$ (upper diagonal shaded area). IME lie mostly outside the iron-group zone. The outer Si velocity is similar for all SNe except HVG SNe. The mass enclosed by IMEs represents the total burned mass. When all SNe are included the average value is ~1.05 ± 0.09 $M_\odot$ (upper horizontal shaded area). Excluding HVG SNe the value is ~1.01 ± 0.05 $M_\odot$ (horizontal line). Both values are independent of $\Delta m_{15}(B)$. For a version of this plot with SN names and a bar diagram, see figs. S2 and S3.

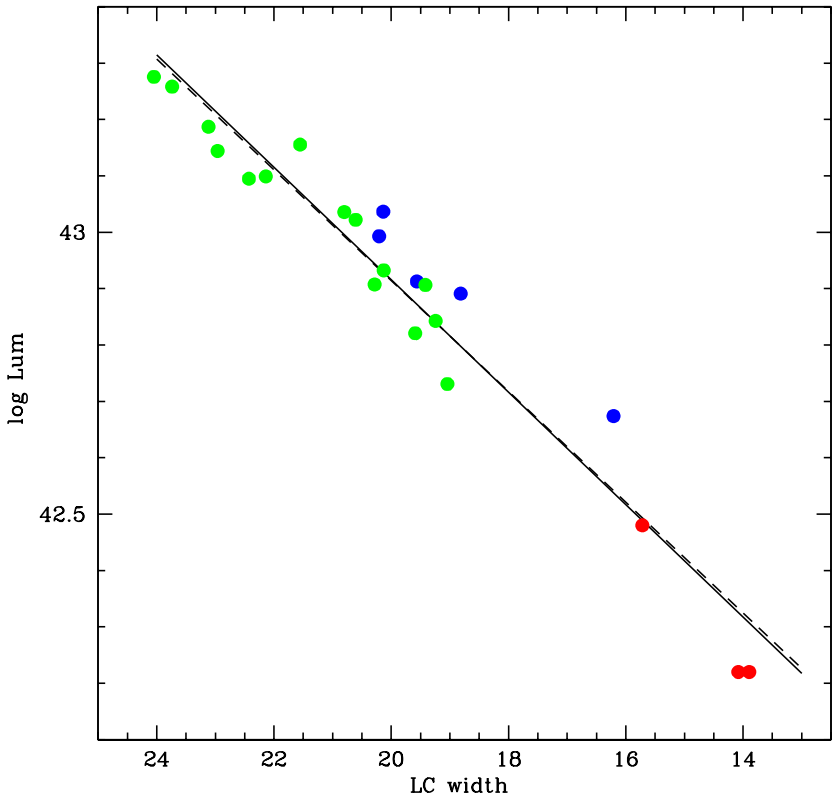

Figure 2: Observed and synthetic luminosity-decline-rate relations for the SNe in our sample. Colors indicate velocity evolution as in Fig. 1. The peak luminosity L was computed from M(^{56}Ni) as $L = 2 \times 10^{43}\ M(^{56}\mathrm{Ni})$ (*28*). Observed bolometric light-curve (LC) widths were obtained from observed rise and decline times (*29*) as $T = (t_{-1/2} + t_{+1/2})$. When $t_{-1/2}$ is missing, it was estimated from the relation between $t_{-1/2}$ and $\Delta m_{15}(B)$ derived from the other SNe. The dashed line is a linear regression between luminosity and observed LC width for the seven SNe common to our sample and that of (*29*). Synthetic bolometric LC widths were obtained assuming that: (i) The LC width τ depends on ejected mass M_{ej}, kinetic energy E_{k}, and opacity κ as: $\tau \propto \kappa^{1/2} E_{\mathrm{k}}^{-1/4} M_{\mathrm{ej}}^{3/4}$ (*21*). (ii) For all SNe, $M_{\mathrm{ej}} = M_{\mathrm{Ch}}$. The W7 (*1*) density-velocity distribution was used. (iii) The explosion kinetic energy depends on the burning product: $E_{\mathrm{k}} = [1.56M(^{56}\mathrm{Ni}) + 1.74M(\mathrm{stableNSE}) + 1.24M(\mathrm{IME}) - 0.46] \times 10^{51}$ erg (*17*). (iv) Opacity is mostly due to line absorption (*30*). Accordingly, NSE elements contribute much more than IMEs because their atomic level structure is more complex. The opacity was therefore parametrised according to the abundances of different species: $\kappa \propto M(\mathrm{NSE}) + 0.1\,M(\mathrm{IME})$ (*16*). To compare the parametrized LC widths τ to observed values T, a scale factor $x = T/\tau$ was computed for each of the seven SNe common to our sample and that of (*29*). The average factor, $x = 24.447$, was used to scale all SNe. Dots show the individual SNe. The continuous line is the linear regression between luminosity and synthetic LC width for our 23 SNeIa sample. For a version of this plot with SN names, see fig. S4.